Journal of Power Sources 284 (2015) 146–153

Contents lists available at ScienceDirect

Journal of Power Sources

journal homepage: www.elsevier.com/locate/jpowsour

Nanoporous graphene materials by low-temperature vacuum-assisted thermal process for electrochemical energy storage

Hao Yang [a], Santhakumar Kannappan [b], Amaresh S. Pandian [c], Jae-Hyung Jang [b], Yun Sung Lee [c], Wu Lu [a, b, *]

[a] Department of Electrical and Computer Engineering, The Ohio State University, Columbus, OH 43210, United States
[b] Department of Nanobio Materials and Electronics, Gwangju Institute of Science and Technology, Gwangju 500-712, Republic of Korea
[c] Faculty of Applied Chemical Engineering, Chonnam National University, Gwangju 500-757, Republic of Korea

HIGHLIGHTS

- A low temperature vacuum assisted thermal process is developed for synthesis of graphene reduced oxide.
- The synthesized reduced graphene oxide materials have a mesoporous surface with a pore size around 3.77 nm.
- The supercapacitors exhibited a specific capacitance of 284.5 F/g and an energy density of 131 Wh/kg.
- The exfoliation mechanism study reveals that the pressure of evolved gases is strong enough to initialize the exfoliation.

GRAPHICAL ABSTRACT

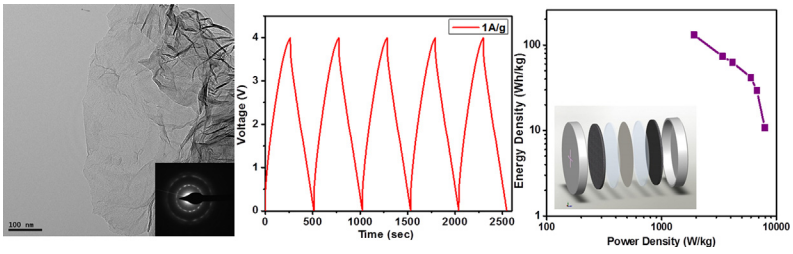

ARTICLE INFO

Article history:
Received 5 February 2015
Accepted 3 March 2015
Available online 5 March 2015

Keywords:
Supercapacitors
Graphene
Electrochemical performance
Energy storage

ABSTRACT

Graphene supercapacitors with a high electrode surface area have great potential in efficient energy storage. For practical applications, it is critical to develop highly-manufacturable methods to synthesize graphene nanosheets with high ion accessibility and uniform pore-sizes. Here we demonstrate a nontoxic approach for graphene synthesis which involves a low vacuum annealing at an easy-to-reach temperature. The supercapacitors based on the low-temperature exfoliated graphene materials show excellent electrochemical performance superior to those synthesized by high-temperature methods. Our investigation presents an efficient, yet industry-compatible and low cost way that can be scaled up for mass production of graphene for electrochemical energy storage application.

1. Introduction

Energy exists in various forms in nature being discovered and exploited with the development of human intellect. With the discovery of each energy source such as fire, fossil, nuclear reaction, the human civilization was given a strong impetus. Meantime, researchers never stop developing the techniques of storing and releasing the collected energy to power a variety of systems. One of the great challenges is to develop high power, highly efficient, environmentally friendly and low cost energy storage devices for immediate burst power applications, like elevator emergency stop, crane lifting operation, renewable energy collection, turbine pitch

* Corresponding author. Department of Electrical and Computer Engineering, The Ohio State University, Columbus, OH 43210, United States.
E-mail address: lu.173@osu.edu (W. Lu).

http://dx.doi.org/10.1016/j.jpowsour.2015.03.015
0378-7753/

control, electric vehicle acceleration, regenerative braking, uninterrupted power supply, and so on. Among all the efforts, development of supercapacitors is a milestone due to the fact that they can offer an extremely high charge–discharge rate, long cycle life, and high energy conversion efficiency [1–3]. By using nanoscale separation of double-layer charges at the electrochemical interface between electrode surface and electrolyte, the energy can be stored or released very efficiently via ion transport [4]. Supercapacitors based on this mechanism are called electric double-layer capacitors (EDLCs). Typically, EDLCs exhibit lower specific capacitance than faradaic supercapacitors or pseudocapacitors which are governed by electrosorption and surface redox reactions [4,5]. However, the ion transport in EDLCs is faster and more reversible than the redox reaction in pseudocapacitors. The energy density of the current commercial supercapacitors, which are based on porous activated carbon electrodes, is around 3–5 Wh/kg [6,7]. On the other hand, the typical energy density of lead acid batteries is 30–50 Wh/kg [8–10]; 60–80 Wh/kg for nickel-metal hydride batteries [9,11], and 100–275 Wh/kg for lithium ion batteries [7,12]. Thus, research efforts have been focused on improving the energy density to the level of battery technologies without sacrificing cycling stability, power density and manufacturing cost.

The capacity of supercapacitors is highly confined by the morphology and electrochemical properties of electrode materials, and consequently there has been a dramatic increase in the study to improve the electrochemical performance of electrode materials. Conducting polymers, such as polyaniline, polypyrrole, polythiophene and their derivatives, undergoes a fast redox reaction providing an excellent specific capacitance (up to 950 F/g) [13], and also show high conductivity (0.1–500 S/m) through a conjugated bond system along the polymer backbone [14]. Unlike the highly cyclable EDLCs, conducting polymers based pseudocapacitors start to degrade under one thousand cycles as a result of the volume change caused by the intercalation and deintercalation of ions [14,15]. Alternatively, supercapacitors based on metal oxides like RuO_2 have been intensively studied due to their high theoretical specific capacitance of 1358 F/g [16]. However, the poor electrical conductivity, limited electrolyte compatibility, cycling instability and high cost have prevented those metal oxide supercapacitors from commercialization. Therefore, it has been of great interest to develop an electrode material with high specific capacitance, electrochemical stability and cost effectiveness. Carbon materials, due to their various microtexture and processability, are more attractive than other materials. Both the single-walled carbon nanotubes and multi-walled carbon nanotubes have been investigated for electrodes in electrochemical capacitors due to their nanoscopic pore size distribution, low resistivity, and high chemical stability [17,18]. Unfortunately, the carbon nanotubes cannot exhibit satisfactory specific capacitance until conducting polymers are added [19].

Since first reported in 2004 [19], graphene has attracted great attention due to its appealing electrical properties [20–25], physical and chemical stabilities [26,27], and high surface area [28–30] arising from its honeycomb lattice structure, thus leading to many potential applications such as large area displays and electrochemical energy storage [25]. Ideally a monolayer of sp^2 bonded carbon atoms can reach a high specific capacitance as well as a surface area of 2675 m^2/g [31,32]. Thus, graphene materials are expected to have a much better electrochemical performance than activated carbons, carbon nanotubes, and other carbon materials. The mechanical exfoliation and chemical vapor deposition approaches can create high quality monolayer or few layer graphene, but they are not suitable for electrochemical energy storage applications due to the planar morphology, high cost, and low production throughput. In addition, because of the hydrophobic nature of graphene and its strong tendency to agglomerate, several alternative graphene synthesis processes for electrochemical energy storage have been developed like chemical reduction [33,34], microwave irradiation [35], thermal annealing [36,37], and powerful sonication [38]. Though tremendous progress has been made, the involved reducing agents such as hydrazine and dimethylhydrazine are very hazardous and toxic, and the energy densities of graphene electrodes are still significantly lower than those of typical Li-ion batteries. The key challenge is to develop a cost effective process of graphene materials that can be scaled up for high throughput production of supercapacitors with superior energy and power density [25]. The critical requirements for such materials are uniform pore size, high ion accessibility and minimal restacking or agglomeration. In this work, we develop a simple, yet highly efficient and scalable method to produce nanoporous graphene materials for energy storage devices. Using synthesized graphene as electrode materials, we demonstrate supercapacitors with an energy density of 131.6 Wh/kg and a specific capacitance of 284 F/g.

2. Experiments

2.1. Preparation of graphite oxide (GO)

GO was prepared by oxidizing the graphite powder with modified Hummer's method [39]. The GO is heavily oxygenated with a basal plane mainly occupied by C═O, C–OH and COOH groups. 20 g of graphite powder, 10 g of $K_2S_2O_8$ and 10 g of P_2O_5 were mixed into a solution of 30 mL concentrated H_2SO_4 at 80 °C, and the mixture was allowed to react for 6 h. The product then was washed with distilled water until the pH value became neutral followed by filtration. The oxidized graphite was put into 460 mL of H_2SO_4 at 0 °C using an ice bath. 60 g of $KMnO_4$ was added gradually with continuous stirring and cooling to keep temperature below 35 °C. 920 mL of distilled water was added after 2 h. In another 2 h, 2.8 L of distilled water and 50 mL of 30% H_2O_2 stopped the reaction and the color of the solution turned into yellow. To remove metal ions, the solution was centrifuged and washed with 10% HCl and then distilled water. A two weeks dialysis was performed to completely get rid of metal ions.

2.2. Preparation of vacuum-annealed graphene (VAG)

The thermal exfoliation of graphene through oxidation, reduction and expansion presents an efficient way of producing graphene sheets. According to the comparison between the Arrhenius dependence of reaction rate and diffusion coefficient calculated by Knudsen theory, a critical temperature of 550 °C is suggested for the initialization of exfoliation [40]. However, experimentally a high temperature above 1000 °C and rapid heating (~2000 °C/min) are necessary for yielding single graphene sheets [36,40]. The high energy consumption is of great safety concern which makes it not a practical approach for mass production of graphene. In graphene electrodes for electrochemical energy storage applications, slight agglomeration is acceptable as a trade-off between performance and cost effectiveness.

The process we have developed involves a one step process using vacuum-assisted annealing to exfoliate the stacked GO sheets and remove the oxide groups. When heated around 160 °C, the oxide groups decompose producing gases (CO_2 and H_2O) [41]. Here, the GO was left in vacuum oven at the temperature of 150 °C and the pressure of −76 cm Hg for 4 h. The evolved gases cause a rapid expansion inside the stacked layers, while the vacuum offers an outward pulling force on GO sheets accelerating the exfoliation process (Fig. 1a). The process can be visually observed (Fig. 1a) with the color change from brown to black (related to reduction) and

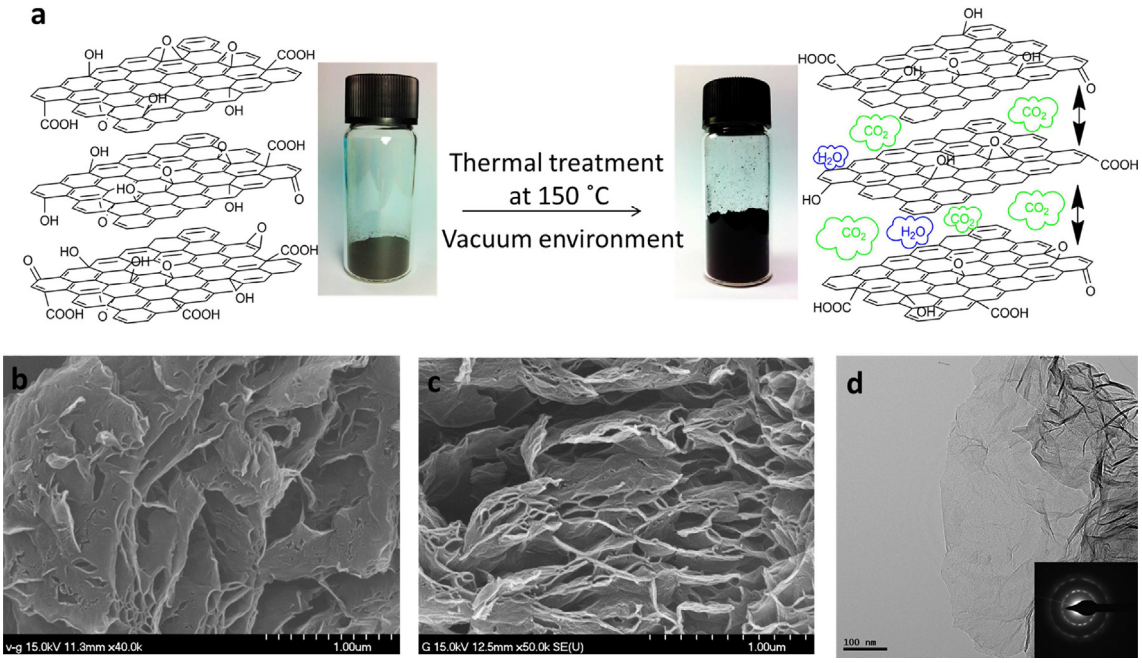

Fig. 1. (a) Schematic of the synthesis process of VAG material. With the help of the vacuum offering an outward force, the pressure of the evolved gases can generate enough pressure to overcome the van der Waals force in the material. FESEM (b), SEM (c) and TEM (d) images show the morphology of the VAG materials at different magnification level. The inset of (d) is the selective area electron diffraction pattern for typical restacked graphene sheets.

large volume expansion (related to exfoliation). It is worthy to mention that the reduction and exfoliation take place simultaneously in this approach avoiding separate treatment for each of them. In this work, we show that the GO can be effectively reduced and exfoliated supported by the material characterization data and electron microscopy images. The superior performance on the capacity of charge/energy storage is demonstrated on supercapacitors based on the VAG electrodes.

2.3. Material characterization

The morphology of the synthesized VAG material was characterized by field emission scanning electron microscopy (FESEM, HITACHI S-4700, Japan) and high-resolution transmission electron microscopy (HRTEM, TECNAI F20), respectively. The measurement of nitrogen adsorption isothermal was done at 77 K by low temperature nitrogen adsorption surface area analyzer (ASAP 2020, Micromeritics Ins, USA). The diffraction patterns were tested by high resolution X-ray diffractometer (HR-XRD, Rigaku, Japan) with Cu Ka radiation ($\lambda(K_\alpha) = 1.54056$ Å). Raman spectra were obtained with Horiba Jobin-Yvon, France with 514 nm Ar^+ ion laser excitation source at 10 mW. X-ray photoelectron spectroscopy (XPS) was done on MULTILAB 2000 system (SSK, USA). The Fourier transform infrared (FTIR) study was also carried out to examine the vibrational characteristics of graphene using an IR Prestige-21, Shimadzu, Japan.

2.4. Electrode preparation and cell assembly

To prepare the electrode, graphene material was mixed with Ketjen black and teflonized acetylene black (TAB) followed by pressing on a nickel mesh (1.6 cm diameter) under a pressure of 300 kg/cm^2. The mass of each electrode is 1 mg. After preparation, each electrode was vacuum dried at 130 °C for 5 h. To evaluate the electrochemical performance of VAG electrodes, supercapacitors were assembled in symmetrical cell geometry with two electrodes. The devices were assembled in CR2032 cell cases with two identical VAG electrodes in an argon filled glove box. A porous polypropylene film (Celgard 3401) was used as the separator. The electrolytes used are ionic liquid $EMIMBF_4$.

2.5. Electrochemical measurement

The cyclic voltammetry (CV) was carried out with CHI760D (CH Instruments, Inc., USA) at scan rate from 5 mV/s to 100 mV/s. The electrochemical impedance spectroscopy (EIS) measurement was analyzed within a frequency range of 100 kHz to 0.1 Hz at an open-circuit potential with an a.c. amplitude of 10 mV with a Zahner Electrochemical Unit 1M6e (Zahner, Germany). Galvanostatic charge/discharge (GCD) cycling of the cells was performed at current density from 1 A/g to 8 A/g with a battery tester (NAGANO, BTS-2004H, Japan).

3. Results and discussion

3.1. Material characterizations

The FESEM and SEM images (Fig. 1b, c) show the morphology and structural features of graphene materials synthesized by the low temperature vacuum-assisted annealing with a “comb-like” network. They reveal the successful exfoliation under which a large area of restacking carbon layers has been peeled off resulting in obvious gaps between them. And this network leads to a better utilization of surface area buried beneath the VAG electrode surface. The TEM image in Fig 1d shows the typical morphology of VAG sheets, where the agglomeration is very limited. The selected-area electron diffraction (SAED) pattern (inset of Fig. 1d) shows dotted concentric rings that indicates the crystalline phase of VAG.

The XRD pattern of GO powder in Fig. 2a shows an intense peak around $2\theta = 12.06°$ (interlayer spacing $d = 7.31$ Å) corresponding to the (002) plane of GO. The removal of oxygen groups in GO by low-temperature vacuum annealing process leads to the broadening

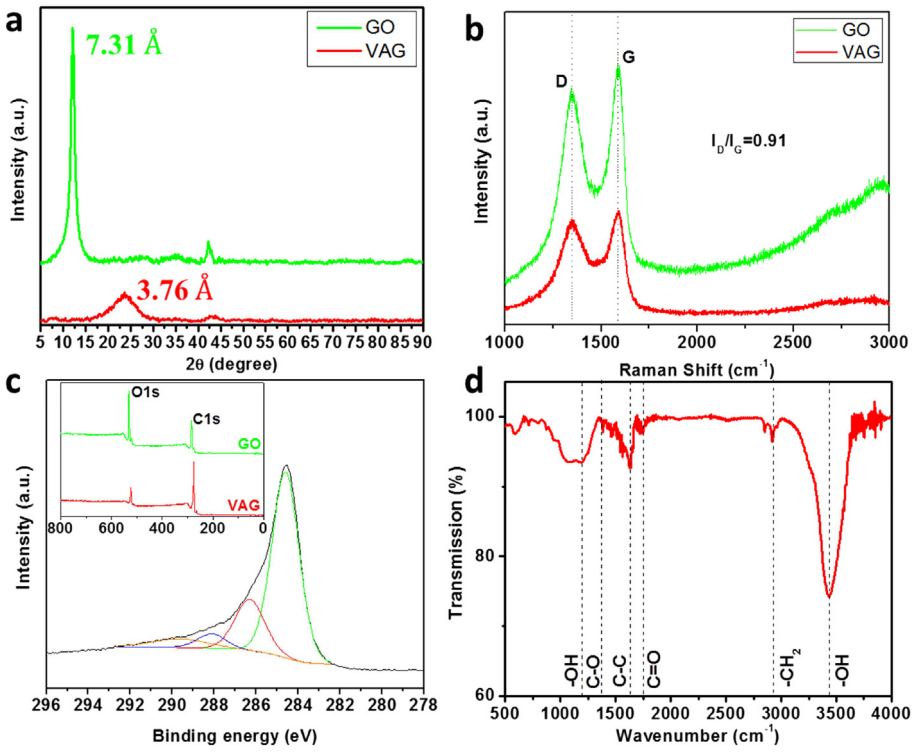

Fig. 2. Material characterization results of the VAG. (a) XRD comparison between GO and VAG samples showing the interlayer spacing decrease after the exfoliation and reduction, which suggests the removal of oxygen groups. (b) Raman spectrum of the VAG sample. (c) XPS C1s spectrum of the VAG sample and the inset is the comparison between GO and VAG. (d) FTIR spectrum of the VAG powder.

and shifting of the peak to $2\theta = 23.60°$ resulting in a reduced interlayer spacing of 3.76 Å.

The highly ordered graphite typically has two visible Raman bands: the G band (~1580 cm^{-1}) caused by in-phase vibration of graphite lattice and the weak D band (~1355 cm^{-1}) resulted from slight disorder [42]. Fig. 2b shows the Raman spectra of GO and VAG. Due to the amorphization during the oxidation process, the GO contains a certain amount of sp^3 bonded carbons [43]. Thus, a broad and relatively intense D band is commonly observed as well as a broad G band [44]. Along with the transition of GO to VAG, it undergoes some defects and vacancies [36,40,44], like the 5-8-5 defects composed of two pentagonal rings and an octagonal ring [45], and Stone-Wales defects (5-7-7-5 rings) [46]. The D band of VAG is observed at around 1350 cm^{-1} and the G band is around 1594 cm^{-1} with $I_D/I_G = 0.91$. In VAG, the G band shifts to the higher frequency region compared with graphite. The blue shift of G band could be caused by the presence of double bonds which resonate at high frequencies than G band [44]. The merge of the defects induced D′ band at 1620 cm^{-1} [42,47,48] or the unmodified graphitic areas may also contribute to the shift [49].

The inset of Fig. 2c shows the XPS spectra of GO and VAG. The spectra reveal the presence of carbon and oxygen with no other detected hetero element and the C/O ratio is 6.08, which compares favorably with rGO materials by other reduction methods at slightly higher temperatures [50,51]. For the C1s peak of VAG, the main peak attributed to the non-oxygenated carbon locates at 284.6 eV. And the other peaks at 286.4, 288.2, and 289.7 eV are assigned to the oxygen containing groups C–OH (or C–O–C), C=O and COOH respectively [52]. The existence of C–O–C which is widely seen in the graphene oxide system has a similar C1s binding energy to C–OH [53]. While further reduction of oxygen should result in better electrochemical performance, it is worthy to point out that it is always a compromise between device performance and complexity and manufacturability of the processes. The key point, though, is to demonstrate excellent electrochemical performance using a more manufacturable and low cost process.

The FTIR spectrum of VAG (Fig. 2d) shows strong absorption peaks at approximately 3433 cm^{-1} and 1637 cm^{-1}. Those two peaks are assigned to the stretching and bending vibration of OH groups in the water molecules absorbed on VAG. The weak peaks at 1719 cm^{-1}, 1385 cm^{-1} and the band between 1050 and 1190 cm^{-1} are due to the C=O, C–O and C–OH stretching vibration in COOH groups [54,55] presented at the edges. This indicates a substantial removal of the oxygen containing groups. Finally, the asymmetric and symmetric stretching vibrations of CH_2 are observed at 2850 and 2918 cm^{-1}, while the peak at 1626 cm^{-1} can be contributed to the skeletal vibration of C=C [56].

The surface properties can be characterized by the N_2 adsorption isotherm measurement (Fig. 3a). The type IV adsorption isotherm curve and a hysteresis loop indicate the presence of slit-shaped mesopores. According to Barret–Joyner–Halenda (BJH) methods, the pore size distributes abruptly in the range of 3.77–4.27 nm. Based on the Brunauer–Emmett–Teller (BET) theory, the resulted surface area is determined to be around 500 m^2/g. Theoretically the single layer graphene has a surface area of 2675 m^2/g [33]. However, the reported surface areas vary in a considerably wide range of 300–3000 m^2/g [33–35]. The inconsistency could be the result of the difference in surface area characterization methods, the agglomeration variation of graphene sheets from synthesis methods, or residual adsorbed solvents or water. Note that the BET surface area doesn't necessarily reflect the actual accessible sites that electrolyte ions can reside on. Thus, the device performance can't be evaluated by simply taking account of BET surface area. Instead, the electrochemical performance can only be characterized by CV, GCD and EIS in assembled supercapacitor cells.

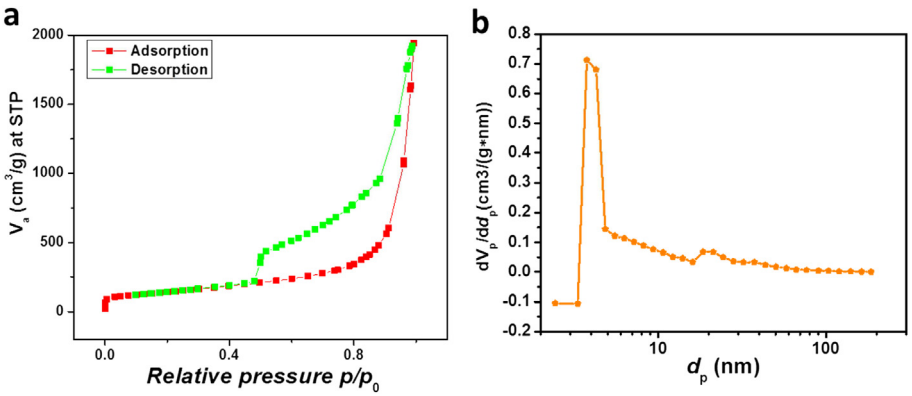

Fig. 3. (a) Nitrogen adsorption/desorption plot at 77.4 K of the VAG sample. The type IV adsorption isothermal curve with a hysteresis loop suggests the near cylindrical or slit geometry of major pores. (b) Pore-size distribution of the VAG sample.

3.2. Exfoliation mechanism study

For a conservative estimation of the gas pressure, we consider that the major mass loss of GO during thermal treatment is contributed by CO_2 (44 g/mol) instead of H_2O (18 g/mol). In order to estimate the pressure that can be generated by the evolution of CO_2, a few assumptions are made here: the oxygen containing groups are homogeneously distributed on the GO surface; all the CO_2 have been released; the spacing between GO sheets doesn't change within the GO sheets. The thermogravimetric analysis (TGA) data (Fig. 4) provides the weight loss of the GO during heating, thus leading to the mass of generated CO_2 at different temperatures. By dividing the mass of CO_2 by the molar mass, we can get the number of CO_2 molecules in the gaps between restacked GO sheets. The spacing of the gaps is extracted by subtracting the interlayer spacing 0.731 nm from XRD data by the single layer graphene thickness 0.335 nm [57]. By multiplying the spacing and the ideal surface area of graphene, the volume of gaps per mass of the material can be extracted. With the number of CO_2 molecules and the volume of gaps, the pressure of the evolved CO_2 is obtained to be 7.43 MPa at a temperature of 150 °C based on the ideal gas law.

To evaluate the pressure required to exfoliate the GO sheets, we assume that the GO material is a layered planar system with infinitely extended area. According to Lifshitz's theory, for two parallel infinitely extended slabs with a thickness of a, the interaction free energy G (per unit area) to bring them from infinite separation to finite separation l is [58]:

$$G_{AmB} = -\frac{A_{Ham}}{12\pi}\left[\frac{1}{l^2} - \frac{2}{(l+a)^2} + \frac{1}{(l+2a)^2}\right] \quad (1)$$

where A_{Ham} is the Hamaker coefficient. If we consider GO a restacked multilayer system with very large slab thickness $a \to \infty$, the pressure to overcome van der Waals force can be approximated as:

$$P = \frac{\partial G}{\partial l} = \frac{A_{Ham}}{6\pi l^3} \quad (2)$$

Since the pressure is inversely proportional to l^3, the higher interlayer distance of GO than graphite leads to a weaker van der Waals force to overcome, which explains why oxidized system is preferred in the exfoliation. This also implies that once the split between layers is initiated, the rest exfoliation occurs in an accelerating pace. According to Lifshitz's theory, in the non-retarded region [59], the evaluated Hamaker coefficient for the GO system is approximately 1.76 zJ. Based on Equation (2), the estimated pressure to break the van der Waals binding between GO layers is 1.51 MPa. This is significantly smaller than the previous extracted gas pressure. This, however, doesn't mean that the vacuum is not required. In a practical case, the initiation of exfoliation would require a higher pressure due to the smaller interlayer spacing along the edges and capillary forces across the GO plane. Also, vacuum environment isolates the GO from the oxygen in the air. This ensures that there is no or minimal reoxidation happening during the exfoliation process. Thus, the evolution of CO_2 and water vapor along with the help from vacuum environment can overcome the van der Waals forces between GO sheets.

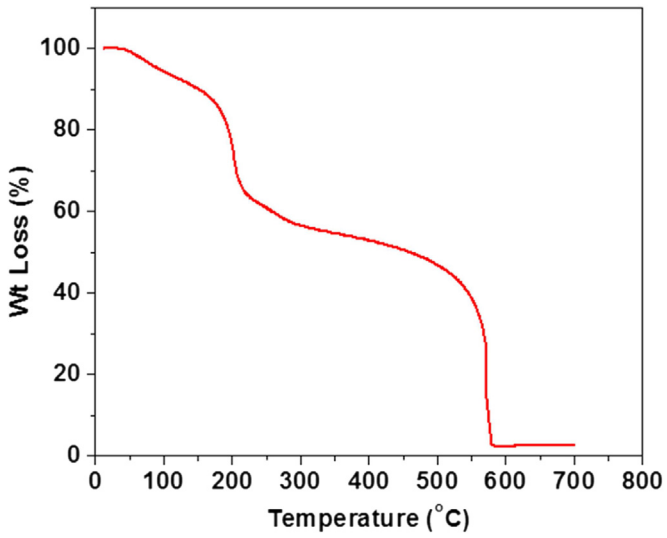

Fig. 4. TGA curves of GO showing the weight loss at different temperatures.

3.3. Electrochemical measurement

In order to demonstrate the energy storage performance of VAG electrodes, the graphene supercapacitors were assembled in a symmetrical cell using ionic liquid $EMIMBF_4$ electrolyte. The prepared graphene electrodes still maintain a porous surface as shown in Fig. 5. The performance of supercapacitors was evaluated with CV, GCD and EIS measurements (Fig. 6). Fig. 6a shows the schematic of the components in a symmetrical supercapacitor cell. Unlike the aqueous electrolyte, ionic liquid, $EMIMBF_4$, is not only highly conductive (12 mS/cm), but also electrochemically stable with a potential window up to 4.3 V [60]. According to the relationship

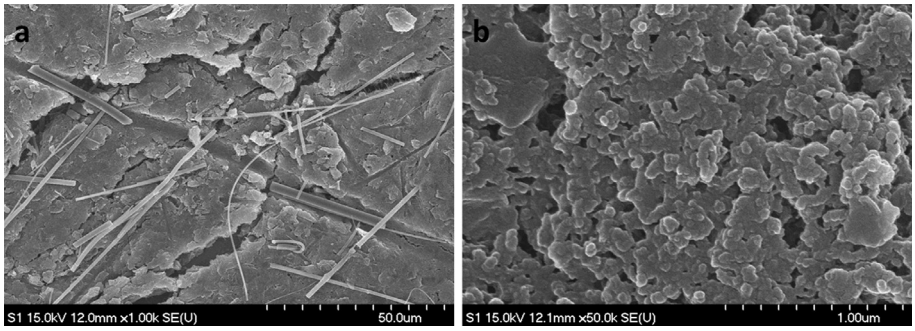

Fig. 5. SEM images of graphene electrode. (a) A SEM image shows the surface of prepared electrode. (b) A high magnification SEM image reveals the porous structure, with which the graphene electrode can provide a high surface area for the access of electrolyte.

$E = CV^2/2$, the wide potential window brings a significant benefit to the improvement of the energy density for supercapacitors. Additionally, the high conductivity can contribute to the reduction of internal resistance resulting in a high power density. The CV curves of VAG electrodes at scan rates from 5 mV/s to 100 mV/s are shown in Fig. 6b. The CV curves show no peaks related to redox reactions implying that the device is charged/discharged at near constant rate over the whole cycle. Because of the relationship $I(t) = C(dV/dt)$, the current will retain a constant value for ideal capacitors. The marginal current response of the charging or discharging is dependent on the electrolyte and internal resistance as well as the scan rate [61]. At low scan rates, the VAG electrodes show almost ideal capacitive behavior in ionic liquid. As the scan rate increases, the shape of CV deviates slightly from a rectangular shape. The repeatability of CV curves and small marginal effect are attributed to the kinetic reversibility and electrical conductivity, respectively. Fig. 6c presents the GCD curves with constant current density from 1 to 4 A/g. The initial voltage drop of discharging is attributed to the voltage loss across internal resistance.

As commonly used in previous reports [4,62], the following equation is used to extract the specific gravimetric capacitance from GCD curves.

$$C_s = \frac{4C}{m} = \frac{4I\Delta t}{m\Delta V} \tag{3}$$

where C is the measured capacitance of the two-electrode cell ($1/C = 1/1/2mC_s + 1/1/2mC_s$), I is the constant current, Δt is the discharging time (except the donation of equivalent series resistance (ESR)), m is the total weight of electrode materials, and ΔV is the voltage drop during discharging process (except the voltage drop on ESR).

Previously, the carbon nanotube-based supercapacitors were reported to have a specific capacitance of 102 F/g for multi-wall carbon nanotube [63] and 180 F/g for single-wall carbon nanotube [64], in contrast to that of tens of F/g for activated carbon based supercapacitors. The maximum specific capacitance for graphene-based supercapacitors is reported to be 265 F/g by El-Kady et al. [65]. Our VAG based supercapacitors showed a value of 284.5 F/g at the current density of 1A/g (Fig. 6d). When

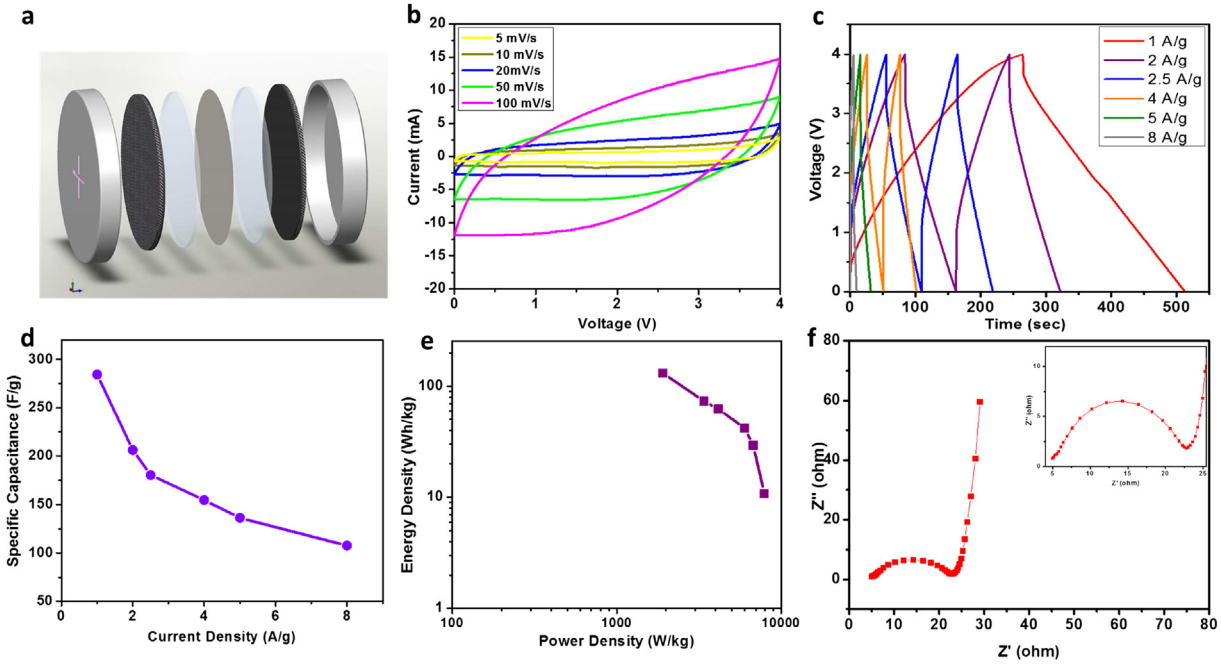

Fig. 6. Electrochemical measurement of VAG based supercapacitor. (a) Schematic of the symmetrical supercapacitor structure. (b) CV curves of VAG electrode in EMIMBF4 at different scan rates. (c) Galvanostatic charge–discharge curves of supercapacitor in EMIMBF4 for different current densities. (d) Specific capacitance versus current density for VAG supercapacitors. (e) Comparative Ragone plots of various energy storage devices and the developed VAG supercapacitors. (f) Nyquist plot extracted from EIS measurement data. The inset is the enlarged high frequency region which shows a shape of semicircle.

Table 1
Comparison of devices in this work with reported graphene supercapacitors based on electrode weight or volume.

Material	Electrolyte	Current density	Specific capacitance	Energy density	Power density	Reference# in the manuscript
Curved graphene	$EMIMBF_4$	1 A/g	154.1 F/g (46.2 F/cm^3)	85.6 Wh/kg (25.68 Wh/L)	1.14 kW/kg (0.34 kW/L)	[33]
a-MEGO	Organic electrolyte	1 A/g	166 F/g (60 F/cm^3)	~70 Wh/kg (23 Wh/L)	N/A	[62]
LSG	Organic electrolyte	~1 A/g	276 F/g (13.2 F/cm^3[a])	28.33 Wh/kg (1.36 Wh/L[a])	N/A	[65]
EM-CCG film	Organic electrolyte	1 A/g	167.1 F/g (208.9 F/cm^3)	88.24 Wh/kg (110.3 Wh/L)	6.88 kW/kg (8.6 kW/L)	[67]
VAG	$EMIMBF_4$	1 A/g	284.5 F/g (78.31 F/cm^3)	131.6 Wh/kg (36.23 Wh/L)	19.03 kW/kg (5.24 kW/L)	This work

[a] These two volumetric values are calculated based on total cell volume.

increasing the current density, the specific capacitance decrease to 206.1, 180.3, 154.7, 136.3, and 107.7 F/g at current densities of 2, 2.5, 4, 5, and 8 A/g.

The energy densities at different current densities were obtained using the following formula [62,65]:

$$E = \frac{1}{8} C_s V^2 \tag{4}$$

The corresponding power density was calculated according to:

$$P = \frac{E}{\Delta t} \tag{5}$$

The maximum power density at the matched impedance condition was evaluated with [7,62,65].

$$P = \frac{V^2}{4mR_{ESR}} \tag{6}$$

Based on above, the maximum energy density of our VAG supercapacitors is 131.6 Wh/kg at room temperature. Table 1 compares both the gravimetric values and volumetric values of our devices with reported state-of-the-art results at similar current density. Clearly, our supercapacitors exhibited superior gravimetric specific capacitance and energy density than those reported devices synthesized by different methods. Assuming the 30% weight of the packaged supercapacitor cell is from the electrode material, the resulted systematical energy density is 39.5 Wh/kg which is one order higher than the commercial supercapacitors mostly based on activated carbons [66]. Fig. 6e presents the Ragone plot of the VAG supercapacitors, showing the energy density and power density relationship at different current densities. Clearly, the devices exhibited both high power densities and high energy densities. Such outstanding performance on energy storage meets many system applications that the current technologies don't.

The EIS data at different frequencies is analyzed using Nyquist plot in Fig. 6f. It shows a straight line in low frequency region corresponding to the capacitive elements in the cell, and an arc in the high frequency region related to the resistive elements between graphene nanosheets [68,69]. The magnitude of equivalent series resistance (ESR) is 4.7 Ω obtained from the x-intercept of the high-frequency arc [68]. The ESR determines the rate that the cell can be charged/discharged, thus determining the power density. Right after the arc, the short line with nearly 45° slope is due to the impact of Warburg resistance, and is a result of the frequency response of ion diffusion from the electrolyte to the electrode interface [68,70]. The very short Warburg line implies that the VAG nanosheets have a short ion diffusion path [70], and this will lead to an efficient utilization of the porous structure of the VAG. Typically, a vertical line in the low frequency region is an indication of pure capacitive behavior. For our VAG sample, the complex-plane impedance curve shows a close to vertical spike in the low frequency region which suggests the supercapacitors behave as an ideal EDLC. And the maximum power density can be estimated using $P = V^2/4mR_{ESR}$, which results in a value of 265 kW/kg.

This vacuum annealing method to produce graphene is fairly easy to set up and requires no high-temperature environment or reducing gases. The 0.002 mol/g CO_2 emission rate per mass of product makes it an environmentally friendly approach, ideal for industrially producing graphene at tons scale. The pores with uniform pore size in the mesoporous range provide the ions homogeneous adsorption sites to form the EDL improving the ion accessibility, leading to an ultra-high specific capacitance and energy density. Although the high-performance electrolyte's contribution to the energy density is important, the excellent performance of VAG supercapacitors is the result of better ion accessibility.

4. Conclusion

In summary, we synthesized the graphene material through an efficient method for industrial production of graphene for supercapacitors. The material characterization shows that the VAG sheets have a mesoporous surface with a pore size around 3.77 nm and reduced oxide composition with C/O ratio of 6.08, both of which are beneficial for ion adsorption in EDL. The clear electron diffraction pattern combined with electron microscopy images reveals a successful exfoliation and the porous morphology of VAG. The fabricated supercapacitors with the VAG electrodes exhibited a remarkable performance with specific capacitance of 284.5 F/g and energy density of 131 Wh/kg. The outstanding electrochemical performance of the VAG supercapacitors meets the power, energy, and durability requirements of many applications that current energy storage technologies can't. The graphene synthesis process developed in this work can be easily scaled up for high volume manufacturing. The appealing properties of this graphene supercapacitor technology could bring new cardiac in electrochemical energy storage.

Acknowledgments

This work is partially supported by the World Class University program by Korean National Research Foundation (Project No. R31-10026) and National Science Foundation (CMMI-0928888).

Appendix A. Supplementary data

Supplementary data related to this article can be found at http://dx.doi.org/10.1016/j.jpowsour.2015.03.015.

References

[1] M. Armand, J.M. Tarascon, Building better batteries, Nature 451 (2008) 652–657.
[2] H. Wu, G. Yu, L. Pan, N. Liu, M.T. McDowell, Z. Bao, Yi Cui, Nat. Commun. 4 (2013) 1943.
[3] C.M. Park, J.H. Kim, H. Kimc, H.J. Sohn, Chem. Soc. Rev. 39 (2010) 3115–3141.

[4] M.D. Stoller, R.S. Ruoff, Energy Environ. Sci. 3 (2010) 1294–1301.
[5] B.Z. Jang, C. Liu, D. Neff, Z. Yu, M.C. Wang, W. Xiong, A. Zhamu, Nano Lett. 11 (2011) 3785–3791.
[6] P. Simon, Y. Gogotsi, Nat. Mater. 7 (2008) 845–854.
[7] A. Burke, J. Power Sources 91 (2000) 37–50.
[8] A. Burke, Electrochim. Acta 53 (2007) 1083–1091.
[9] P.V.D. Bossche, F. Vergels, J.V. Mierlo, J. Matheys, W.V. Autenboer, J. Power Sources 162 (2006) 913–919.
[10] J. Baker, Energy Policy 36 (2008) 4368–4373.
[11] M. Conte, P.P. Prosini, S. Passerini, Mater. Sci. Eng. B 108 (2004) 2–8.
[12] L. Damen, J. Hassoun, M. Mastragostino, B. Scrosati, J. Power Sources 195 (2010) 6902–6904.
[13] M.E. Roberts, D.R. Wheeler, B.B. McKenzie, B.C. Bunker, J. Mater. Chem. 19 (2009) 6977–6979.
[14] G.A. Snook, P. Kao, A.S. Best, J. Power Sources 196 (2011) 1–12.
[15] A.A. Pud, Synth. Met. 66 (1994) 1–18.
[16] C.D. Lokhande, D.P. Dubal, O.S. Joo, Curr. Appl. Phys. 11 (2011) 255–270.
[17] H. Pan, J. Li, Y.P. Feng, Nanoscale Res. Lett. 5 (2010) 654–668.
[18] Q. Wang, Z.H. Wen, J.H. Li, Adv. Funct. Mater. 16 (2006) 2141–2146.
[19] K.S. Novoselov, A.K. Geim, S.V. Morozov, D. Jiang, Y. Zhang, S.V. Dubonos, I.V. Grigorieva, A.A. Firsov, Science 306 (2004) 666–669.
[20] K.S. Novoselov, A.K. Geim, S.V. Morozov, D. Jiang, M.I. Katsnelson, I.V. Grigorieva, S.V. Dubonos, A.A. Firsov, Nature 438 (2005) 197–200.
[21] Y. Zhang, Y.W. Tan, H.L. Stormer, Philip Kim, Nature 438 (2005) 201–204.
[22] H.B. Heersche, P. Jarillo-Herrero, J.B. Oostinga, L.M.K. Vandersypen, A.F. Morpurgo, Nature 446 (2007) 56–59.
[23] G.M. Rutter, J.N. Crain, N.P. Guisinger, T. Li, P.N. First, J.A. Stroscio, Science 317 (2007) 219–222.
[24] N. Tombros, C. Jozsa, M. Popinciuc, H.T. Jonkman, B.J. van Wees, Nature 448 (2007) 571–574.
[25] X. Fan, W. Peng, Y. Li, X. Li, S. Wang, G. Zhang, F. Zhang, Adv. Mater. 20 (2008) 4490–4493.
[26] S. Stankovich, D.A. Dikin, G.H.B. Dommett, K.M. Kohlhaas, E.J. Zimney, E.A. Stach, R.D. Piner, So T. Nguyen, R.S. Ruoff, Nature 442 (2006) 282–286.
[27] D.A. Dikin, S. Stankovich, E.J. Zimney, R.D. Piner, G.H.B. Dommett, G. Evmenenko, S.T. Nguyen, R.S. Ruoff, Nature 448 (2007) 457–460.
[28] X. Wang, Y. Zhang, C. Zhi, X. Wang, D. Tang, Y. Xu, Q. Weng, X. Jiang, M. Mitome, D. Golberg, Y. Bando, Nat. Commun. 4 (2013) 2905.
[29] K.H. Kim, M. Yang, K.M. Cho, Y. Jun, S.B. Lee, H. Jung, Sci. Rep. 3 (2013) 3251.
[30] L. Zhang, F. Zhang, X. Yang, G. Long, Y. Wu, T. Zhang, K. Leng, Y. Huang, Y. Ma, A. Yu, Y. Chen, Sci. Rep. 3 (2013) 1408.
[31] J. Xia, F. Chen, J. Li, N. Tao, Nat. Nanotech. 4 (2009) 505–509.
[32] Y. Wang, Y. Wu, Y. Huang, F. Zhang, X. Yang, Y. Ma, Y. Chen, J. Phys. Chem. C 115 (2011) 23192–23197.
[33] C. Liu, Z. Yu, D. Neff, A. Zhamu, B.Z. Jang, Nano Lett. 10 (2010) 4863–4868.
[34] S. Park, R.S. Ruoff, Nat. Nanotech 4 (2009) 217–224.
[35] Y. Zhu, S. Murali, M.D. Stoller, A. Velamakanni, R.D. Piner, R.S. Ruoff, Carbon 48 (2010) 2118–2122.
[36] H.C. Schniepp, J. Li, M.J. McAllister, H. Sai, M. Herrera-Alonso, D.H. Adamson, R.K. Prud'homme, R. Car, D.A. Saville, I.A. Aksay, J. Phys. Chem. B 110 (2006) 8535–8539.
[37] M. Jin, T.H. Kim, S.C. Lim, D.L. Duong, H.J. Shin, Y.W. Jo, H.K. Jeong, J. Chang, S. Xie, Y.H. Lee, Adv. Funct. Mater. 21 (2011) 3496–3501.
[38] S. Stankovicha, D.A. Dikina, R.D. Pinera, K.A. Kohlhaasa, A. Kleinhammesc, Y. Jiac, Y. Wuc, S.T. Nguyenb, R.S. Ruoff, Carbon 45 (2007) 1558–1565.
[39] N.I. Kovtyukhova, P.J. Ollivier, B.R. Martin, T.E. Mallouk, S.A. Chizhik, E.V. Buzaneva, A.D. Gorchinskiy, Chem. Mater. 11 (1999) 771–778.
[40] M.J. McAllister, J. Li, D.H. Adamson, H.C. Schniepp, A.A. Abdala, J. Liu, M. Herrera-Alonso, D.L. Milius, R. Car, R.K. Prud'homme, I.A. Aksay, Chem. Mater. 19 (2007) 4396–4404.
[41] S. Eigler, C. Dotzer, A. Hirsch, M. Enzelberger, P. Müller, Chem. Mater. 24 (2012) 1276–1282.
[42] F. Tuinstra, J.L. Koenig, J. Chem. Phys. 53 (1970) 1126.
[43] A.C. Ferrari, J. Robertson, Phys. Rev. B 61 (2000) 14095.
[44] K.N. Kudin, B. Ozbas, H.C. Schniepp, R.K. Prud'homme, I.A. Aksay, R. Car, Nano Lett. 8 (2008) 36–41.
[45] G.D. Lee, C.Z. Wang, E. Yoon, N.M. Hwang, D.Y. Kim, K.M. Ho, Phys. Rev. Lett. 95 (2005) 205501.
[46] A.J. Stone, D.J. Wales, Chem. Phys. Lett. 128 (1986) 501–503.
[47] T. Livneh, T.L. Haslett, M. Moskovits, Phys. Rev. B 66 (2002) 195110.
[48] L.G. Cançado, M.A. Pimenta, B.R.A. Neves, M.S.S. Dantas, A. Jorio, Phys. Rev. Lett. 93 (2004) 247401.
[49] D. Graf, F. Molitor, K. Ensslin, C. Stampfer, A. Jungen, C. Hierold, L. Wirtz, Nano Lett. 7 (2007) 238–242.
[50] Y. Zhu, M.D. Stoller, W. Cai, A. Velamakanni, R.D. Piner, D. Chen, R.S. Ruoff, ACS Nano 4 (2010) 1227–1233.
[51] S. Dubin, S. Gilje, K. Wang, V.C. Tung, K. Cha, A.S. Hall, J. Farrar, R. Varshneya, Y. Yang, R.B. Kaner, ACS Nano 4 (2010) 3845–3852.
[52] D. Yang, A. Velamakanni, G. Bozoklu, S. Park, M. Stoller, R.D. Pinner, S. Stankovich, I. Jung, D.A. Field, C.A. Ventrice Jr., R.S. Ruoff, Carbon 47 (2009) 145–152.
[53] C. Kozlowski, P.M.A. Sherwood, J. Chem. Soc. Faraday Trans. 1 80 (1984) 2099–2107.
[54] M. Naebe, J. Wang, A. Amini, H. Khayyam, N. Hameed, L.H. Li, Y. Chen, B. Fox, Sci. Reports 4 (2014) 4375.
[55] L. Shahriary, A.A. Athawale, Int. J. Renew. Energy Environ. Eng. 2 (2014) 58–63.
[56] H. Guo, X. Wang, Q. Qian, F. Wang, X. Xia, ACS Nano 3 (2009) 2653–2659.
[57] Z.H. Ni, H.M. Wang, J. Kasim, H.M. Fan, T. Yu, Y.H. Wu, Y.P. Feng, Z.X. Shen, Nano Lett. 7 (2007) 2758–2763.
[58] V.A. Parsegian, Van der Waals Forces: a Handbook for Biologists, Chemists, Engineers, and Physicists, Cambridge University Press, New York, 2005.
[59] R.F. Rajter, R.H. French, W.Y. Ching, W.C. Carter, Y.M. Chiang, J. Appl. Phys. 101 (2007) 054303.
[60] Sigma Aldrich Chem Files: Ionic Liquids, vol. 5, No. 6, Web-accessed at http://www.sigmaaldrich.com/content/dam/sigma-aldrich/docs/Aldrich/Brochure/al_chemfile_v5_n6.pdf.
[61] J. Jiang, A. Kucernak, Electrochimica Acta 47 (2002) 2381–2386.
[62] Y. Zhu, S. Murali, M.D. Stoller, K.J. Ganesh, W. Cai, P.J. Ferreira, A. Pirkle, R.M. Wallace, K.A. Cychosz, M. Thommes, D. Su, E.A. Stach, R.S. Ruoff, Science 332 (2011) 1537–1541.
[63] C. Niu, E.K. Sichel, R. Hoch, D. Moy, H. Tennent, App. Phys. Lett. 70 (1997) 1480–1482.
[64] K.H. An, W.S. Kim, Y.S. Park, J.-M. Moon, D.J. Bae, S.C. Lim, Y.S. Lee, Y.H. Lee, Adv. Funct. Mater. 11 (2001) 387–392.
[65] M.F. El-Kady, V. Strong, S. Dubin, R.B. Kaner, Science 335 (2012) 1326–1330.
[66] A. Burke, Proc. IEEE 95 (2007) 806–820.
[67] X. Yang, C. Cheng, Y. Wang, L. Qiu, D. Li, Science 341 (2013) 534–537.
[68] B.E. Conway, Kluwer Academic/Plenum Publishers, New York, 1999.
[69] C. Portet, P.L. Taberna, P. Simon, C. Laberty-Robert, Electrochimica Acta 49 (2004) 905–912.
[70] Y. Wang, Z. Shi, Y. Huang, Y. Ma, C. Wang, M. Chen, Y. Chen, J. Phys. Chem. C 113 (2009) 13103.